Nanoscale

PAPER

View Article Online
View Journal | View Issue

Cite this: *Nanoscale*, 2024, **16**, 4703

Super resolution label-free dark-field microscopy by deep learning†

Ming Lei, [a] Junxiang Zhao,[a] Junxiao Zhou, [a] Hongki Lee,[a] Qianyi Wu,[a] Zachary Burns,[a] Guanghao Chen[a] and Zhaowei Liu*[a,b]

Received 27th August 2023,
Accepted 10th January 2024

DOI: 10.1039/d3nr04294d

rsc.li/nanoscale

Dark-field microscopy (DFM) is a powerful label-free and high-contrast imaging technique due to its ability to reveal features of transparent specimens with inhomogeneities. However, owing to the Abbe's diffraction limit, fine structures at sub-wavelength scale are difficult to resolve. In this work, we report a single image super resolution DFM scheme using a convolutional neural network (CNN). A U-net based CNN is trained with a dataset which is numerically simulated based on the forward physical model of the DFM. The forward physical model described by the parameters of the imaging setup connects the object ground truths and dark field images. With the trained network, we demonstrate super resolution dark field imaging of various test samples with twice resolution improvement. Our technique illustrates a promising deep learning approach to double the resolution of DFM without any hardware modification.

Introduction

Label-free imaging techniques have been developed for many decades and widely applied in life science due to their non-invasive and non-toxic approach to biological samples.[1] Dark-field microscopy (DFM) is an important label-free imaging method used in biology, material science and other disciplines, which offers high contrast for a wide range of unstained specimens.[2–4] In DFM configuration, the illumination light beam becomes hollow and oblique after passing through the dark field ring and condenser, in which case only the light scattered by the objects can be detected.[5] As a result, compared with bright-field microscopy, it emphasizes high spatial frequency information and enhances image contrast by highlighting the discontinuities or edges of the object, while the uniform regime remains dark.[6–9] Due to its simple configuration and effective imaging performance, DFM is widely used in revealing outlines of unstained objects. However, the resolution of traditional DFM is diffraction-limited by the detection optics.

Although many excellent super resolution imaging methods have emerged in the past few decades,[10–14] most of them focus on fluorescent imaging and cannot be applied to scattering DFM. Structured illumination microscopy (SIM) is a successful super resolution fluorescent imaging technique using a series of excitation light patterns to encode the high-resolution information into the observed images.[15] Label-free SIM has also been developed in recent years for super resolution imaging but with much less impressive resolution improvement.[16] Fourier ptychographic microscopy using a light emitting diode array to illuminate the label-free sample with different angles achieves resolution improvement with synthesized aperture,[17,18] which could be potentially applied to super-resolution DFM. However, both of them require large modification of the DFM setup and need multiple images to reconstruct a super-resolution image.

In recent years, deep learning (DL) has dramatically influenced the optical imaging field and gained great success in solving the complex inverse problem.[19–23] In contrast to traditional reconstruction methods which typically require explicit mathematical model to find an analytical solution, the DL neural network relies on large datasets to learn by itself to solve the complex inverse problems. Well-designed neural networks have been successfully implemented on reconstructions of many super-resolution imaging techniques.[24–27] Artificial neural network accelerated photoactivated localization microscopy (PALM) reconstructs a PALM image using much less number of sub-images with similar performance, which improved the imaging speed by 26 times.[28] A generative adversarial network (GAN) based framework transforms diffraction-limited input images into super-resolved ones.[29] These neural networks improve the performance of existing imaging methods in either speed or resolution. Nevertheless, in order to optimize their weight and bias parameters for better performance, these neural networks require large training data-

[a]*Department of Electrical and Computer Engineering, University of California, San Diego, 9500 Gilman Drive, La Jolla, California92093, USA. E-mail: zhaowei@ucsd.edu*
[b]*Materials Science and Engineering, University of California, San Diego, 9500 Gilman Drive, La Jolla, California 92093, USA*

† Electronic supplementary information (ESI) available: Supplement 1. See DOI: https://doi.org/10.1039/d3nr04294d

sets which often need laborious experiment work.[30,31] It's also worth noting that researchers has proposed neural networks with no pre-training requirement in certain imaging situations.[32,33] By embedding the forward physical model of imaging process, PhysenNet reconstructs phase image from a single diffraction pattern.[34] Ghost imaging using deep neural network constraint (GIDC) was proposed to increase the spatial resolution in ghost imaging.[35] These physics-informed neural networks avoid the training process at the expense of slow reconstruction speed due to iteration process, which makes real-time super resolution difficult to achieve. More discussion can be found in Supplement 1.

In this study, we propose a CNN based framework specifically designed to improve the resolution of single frame DFM image in real time by retrieving the high spatial frequency information acquired by oblique illumination without any modification to a standard DFM setup. With the known forward process of DFM, we numerically generate the training dataset based on the parameters of the optical setup and require no experimental images. The network is trained on the simulated dataset to retrieve the high spatial frequency information which is encoded in the dark field image. After training the network, we evaluate its performance on unseen simulated images. Afterwards, we experimentally demonstrate the super resolution reconstructions of the dark field images with 100 nm polystyrene beads acquired by a 50×/0.55 NA objective lens. Furthermore, we perform super resolution image reconstruction with dark field images of phase targets and HeLa cells by using the trained CNN. This proposed framework could be applied to any DFM setup for super-resolution with only the knowledge of its illumination and detection parameters, which provides an appealing method for real-time label-free super resolution dark field imaging.

Working principle

In DFM, the central part of the illumination is blocked by the dark field ring, as shown in Fig. 1(a). After passing through the condenser, the illumination light becomes oblique and strikes the sample at an angle, in which case the objective can only collect the scattered light from the object. Following the idea of synthetic aperture,[36,37] the angled illumination pattern corresponding to a ring in Fourier space shifts the high spatial frequency information of the object into the detection bandwidth of the objective, as shown in Fig. 1(b). The highest spatial frequency information attainable by the optical system is restricted by the combination of numerical aperture (NA) of both the illumination and detection objective. The high spatial frequency information is encoded in the diffraction limited dark field image. Thus, a super resolution image may be reconstructed from the detected low resolution one by retrieving the encoded high spatial frequency information (see Fig. 1(c)). Since all the high spatial frequency information of the object overlay and form a single diffraction limited dark field image, retrieving the high resolution image is an extremely ill-posed problem, which is very difficult to solve by traditional optimization methods.

To retrieve the high-resolution information, CNNs can be a good choice because of their great performance in solving complex inverse problems.[38–40] In general case, to train a CNN, a large amount of data from either experiment or simulation is

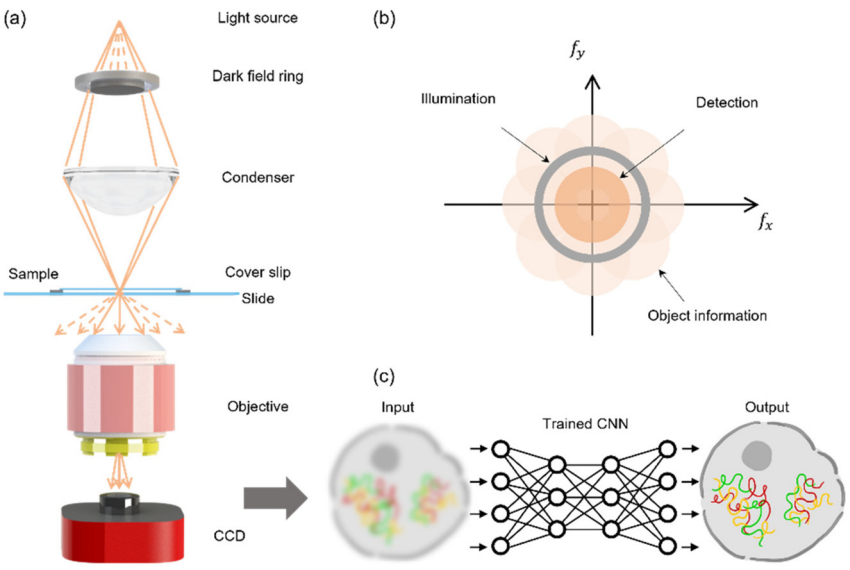

Fig. 1 Principle of CNN based super resolution dark field imaging method. (a) In DFM, oblique cone-shape illumination produced by a dark field ring and a condenser interacts with the sample. Only the scattering light are detected by a charge-coupled device (CCD) camera. (b) Fourier space relationship between the illumination light, detection range, and the actual information collected from the object. The circle centered on the origin indicates the detection range of objective. Each translated information spectrum is centered on the illumination ring. (c) Super-resolved DFM image may be reconstructed by a trained CNN with a single low-resolution dark field image as input.

required to ensure its performance.[41,42] Acquiring enough experimental images for training could be time consuming. Collecting ground truth images is even more difficult in most cases. Here, we propose a simulation method based on the synthetic aperture idea to generate pairs of low resolution and super resolution DFM images with the knowledge of the optics including the objective NA, the illumination angle and the working wavelength.

With the DFM imaging setup shown in Fig. 1(a), we use a 45° angled illumination and a 50×/0.55 NA objective for both simulation and experiment. Under incoherent light illumination, the dark field image can be regarded as a superposition of multiple off-axis images generated by each point source illumination on the illumination dark field ring. Each angled illumination shifts the corresponding high-spatial frequency information of the object into the detection bandwidth of the objective, which is a low-pass filter in the Fourier plane as shown in subset of Fig. 2(a). Considering incoherent illumination, the final low resolution dark field image I_{LR} can be regarded as a sum of images under each angled illumination and approximately calculated as:

$$I_{LR} = \sum_{i=1}^{m} \left|F^{-1}[E_{illu,i}(f_x,f_y) \otimes O(f_x,f_y) \cdot CTF(f_x,f_y)]\right|^2 + n = \sum_{i=1}^{m} \left|F^{-1}[O(f_x + f_{x,i}, f_y + f_{y,i}) \cdot CTF(f_x,f_y)]\right|^2 + n, \quad (1)$$

where $E_{illu,i} = \delta(f_{x,i}, f_{y,i})$ is the Fourier transform of the illumination electrical field of the i-th angle, f_x and f_y are coordinates in Fourier space, $f_{x,i}$ and $f_{y,i}$ are illumination position in Fourier space, $m = 30$ is the total number of illumination angles, $\otimes$ represents convolution operation, O is the object spatial information, F^{-1} represents the inverse Fourier transform, CTF is the coherent transfer function of the detection optics and n is the additive noise. The larger the number m is utilized, the better approximation of real experiment is achieved. The low resolution images are added with white Gaussian noise (signal-to-noise ratio 35) to match the experiment condition before inputting to the neural network.

In a similar way, the super-resolution dark field image I_{SR} containing all detectable high-k information of the object, can be calculated as:

$$I_{SR} = \sum_{i=1}^{m} \left|F^{-1}[O(f_x,f_y) \cdot CTF(f_x - f_{x,i}, f_y - f_{y,i})]\right|^2. \quad (2)$$

As shown in Fig. 2(a), the effective optical transfer function (OTF) of the super-resolved dark field image is a combination of a series of OTFs which are generated by angled illumination. Thus, the highest spatial frequency in the super resolution image corresponds to the combination of the NA of illumination and detection. For each object, simulated I_{LR} and I_{SR} are used as input and label images respectively to train the neural network, as shown in Fig. 2(b) and (c).

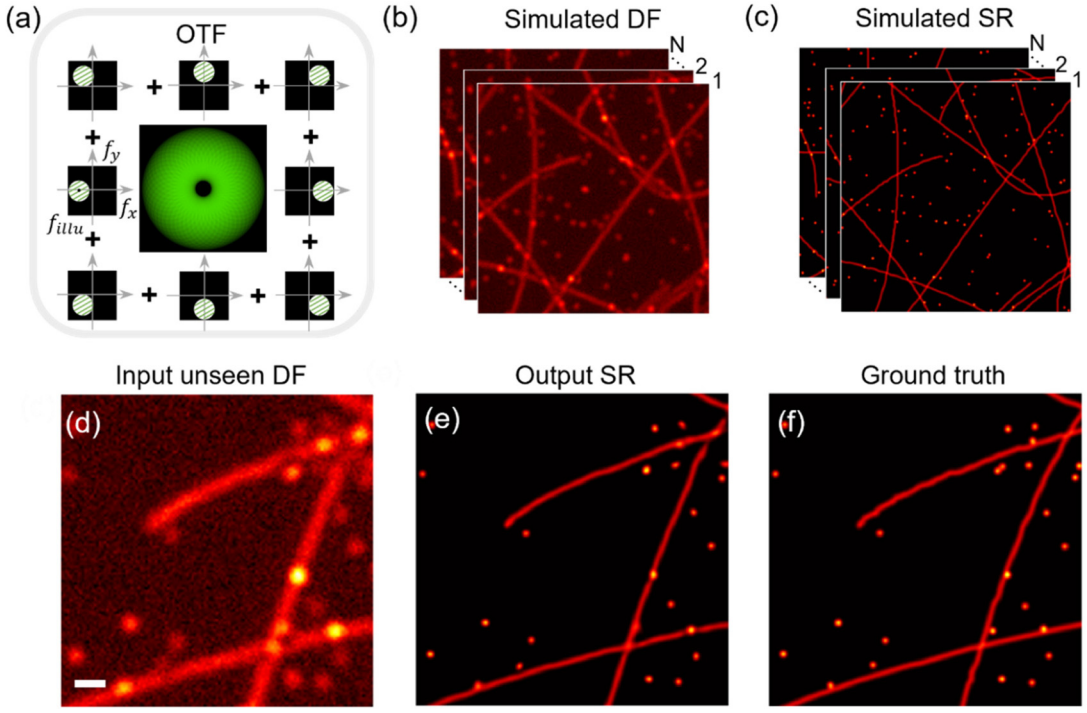

Fig. 2 Simulation method for dataset generation and simulation performance. (a) Effective OTF used in simulation. Each subset image represents the effective OTF of the dark field microscopy under each illumination angle. The big donut-shaped OTF shows the effective OTF of the cone-light illuminated dark field microscopy. (b and c) Computational simulated dark field images and super-resolved dark field images which compose the training dataset. N indicates the size of the dataset. (d) Unseen simulated low resolution dark field image input to the trained network. (e) Output super resolution image of the network. (f) Simulated ground truth super resolution image. Scale bar, 1 μm.

In this work, we use a U-net structure to solve the complex inverse problem. The input low resolution images passing through a down-sampling (encoder) part and an up-sampling (decoder) part are transformed into high-resolution output images. Rectified linear units (ReLU) are used between each convolutional layers to avoid gradient vanishing and exploding problem.[43] We also use adaptive moment estimation (Adam) as optimizer to compute adaptive learning rate for each parameter with the learning rate set to 0.0001.[44] The output super resolution images are compared with the ground truth images using both multi-scale structure similarity index measure (MS-SSIM) and L1-norm.[45] The combined loss function of both MS-SSIM loss and L1 loss is given as:

$$\mathcal{L} = \alpha \cdot \mathcal{L}^{\mathrm{SSIM}} + (1 - \alpha) \cdot \mathcal{L}^{\ell_1} \quad (3)$$

with $\alpha = 0.8$, which is determined after parameter optimization as shown in ESI 1, Fig. S1.† In addition, more information of the U-Net architecture can also be found in ESI 1, Fig. S1.† After training the neural network with simulated dataset which consists of 3000 pairs of low resolution and super resolution images, the unseen dataset is processed by the trained network as a test. The performance of the network is shown in Fig. 2(d–f). By comparing the network output with ground truth image, it is obvious to notice that the diffraction limited features can be clearly resolved in the output image, which match well with the ground truth. We used structure similarity index measure (SSIM) to evaluate the quality of network reconstructed super resolution image, which gives a SSIM of 0.982 ± 0.013 compared to ground truth.

Methods

Dataset preparation and network training

The simulation ground truth images include random distributed scattering particles and fibers generated numerically with different size and length. The low resolution dark field images and super resolution dark field images are then simulated based on eqn (1) and (2) using MATLAB. The neural network architecture is explained in detail in ESI 1, Fig. S1.† Simulation dataset was numerically generated and processed using MATLAB R2020b. The training dataset contains 3000 pairs of simulated images. The batch size was set to be 15. Input images were cropped to be 256 × 256 in size. The training and testing were run on a desktop computer equipped with a NVIDIA GeForce GTX2070S graphic cards and a Core i7-9700K CPU@3.6 GHz.

Polystyrene bead preparation and characterization

Coverslips were cleaned with acetone under sonication for 10 minutes followed by rinsing with isopropanol and deionized water. 100 nm polystyrene beads (Invitrogen, USA) were then drop-casted on the cleaned coverslip and dried before imaging experiment. After the optical imaging experiment, 20 nm Cr was sputtered on the sample for SEM characterization.

Cell preparation

HeLa cells were cultured in Dulbecco's modified Eagle's medium (DMEM) supplemented with 10% fetal bovine serum (Life Technologies, Waltham, MA), 1% penicillin–streptomycin (Life Technologies), and 2 mM glutamine in 5% CO_2 at 37 °C. 2×10^5 cells were seeded in each well of a 6-well plate at which clean BK7 glass substrates were placed. After removing the medium, fixation for 15 minutes with 4% paraformaldehyde solution in phosphate buffered saline (PBS) at 4 °C was followed. The sample was washed with PBS and dehydrated for imaging.

Results

With the neural network trained on simulated dataset, we test its performance over experimental data. The DFM imaging setup shown in Fig. 1(a) is utilized to acquire low resolution dark field images. A 532 nm laser guided by a multi-mode fiber is used for illumination and a CCD camera (iXon 897, Andor) is used to record images. To be consistent with simulation, we use multi-mode fiber vibrated by an eccentric rotating mass motor and long exposure time of camera to reduce the coherency of the illumination. Experiment results with polystyrene beads are shown in Fig. 3. Polystyrene beads with 100 nm diameter are drop-casted onto a glass substrate as

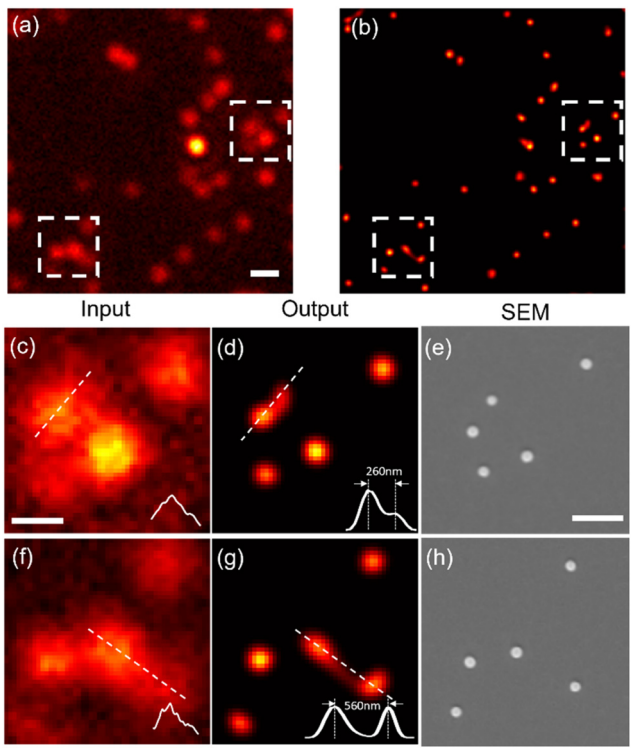

Fig. 3 Trained U-Net performance on experimental data with 100 nm polystyrene beads. (a) Low resolution dark field images. Scale bar, 1 μm. (b) Output of the network. (c, d, f and g) Magnified small region-of-interest. (e and h) SEM ground truth images used for confirming the accuracy of the network output. Scale bar, 500 nm.

imaging object. Two beads with a separation of around 260 nm can be resolved as shown in Fig. 3(d). The network output matches well with the SEM shown in Fig. 3(e). Considering our imaging setup with 50×/0.55 NA objective lens and 45° angled illumination, the maximum effective NA of the imaging setup is 1.26, which agrees well with the resolution in experiment. Compared with the noisy input images, the output images also show that our network has good performance in suppressing the noise.

In addition, we apply the network to DFM images of a phase object (Quantitative phase microscopy target, Benchmark Technologies) including a grating pattern and a 1951 USAF resolution pattern. In this case, we illuminate the sample with a 530 nm LED (M530L4, Thorlabs). Compared with the experiments with polystyrene beads, the phase targets have more complex structures. Nevertheless, as shown in Fig. 4, defects of the phase objects are clearly resolved with a two-point resolution of ~220 nm, which is on the same level as the experiment results shown in Fig. 3.

Next, we apply the same trained network to HeLa cells which have more complex structures and have never been seen by the network. The image acquisition setup remains the same as the experiment in Fig. 3. Compared with the input low resolution images and the denoised low resolution images, the network output images shown in Fig. 5(g–i) clearly resolve the major features of the HeLa cells. As illustrated by the cross-section profile in Fig. 5(g–i), structures with around 280 nm separation are clearly separated. Fourier spectrums of the low-resolution and super-resolution dark field images are then used to confirm the ~2 times resolution improvement, as shown in ESI 1, Fig. S2.†

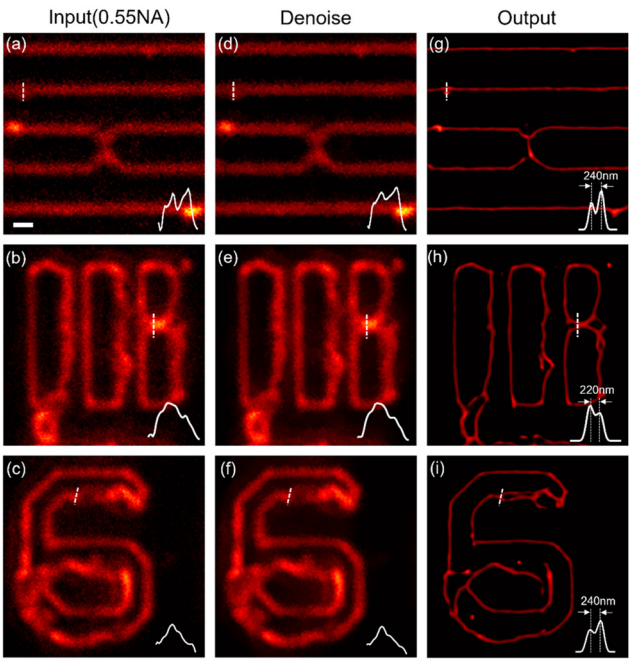

Fig. 4 Trained network performance on experiment data with phase objects. (a–c) Dark field images of the phase object acquired with a 50×/0.55 NA objective. (a) A grating pattern (b and c) USAF resolution targets. (d–f) Denoised low resolution dark field images with nonlocal filtering methods.[46] (g–i) Network output SR images. Scale bar, 1 μm. All the cross-section profiles are magnified twice for better visualization.

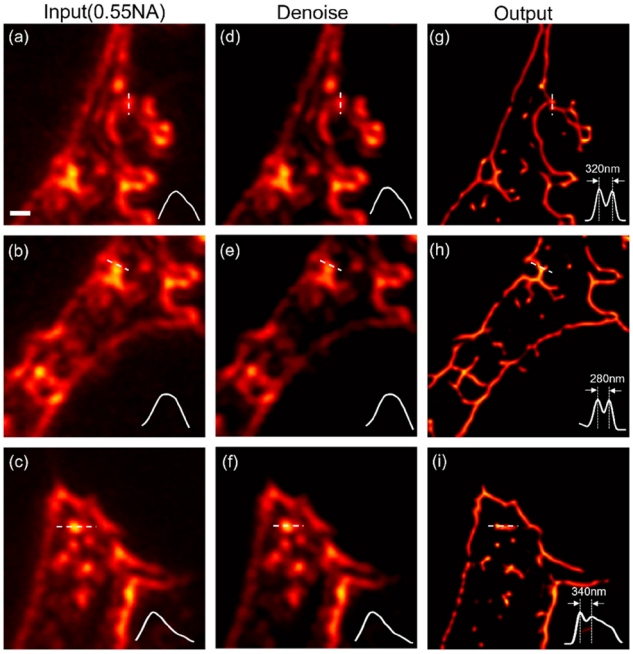

Fig. 5 Trained U-Net performance on experiment data with HeLa cells. (a–c) Dark field images acquired with 50×/0.55 NA objective. (d–f) Denoised low resolution images using nonlocal filtering method. (g–i) Network output. Scale bar, 1 μm. All the cross-section profiles are magnified twice for better visualization.

Discussion and conclusion

Several approaches can be applied to the proposed technique to further improve its performance. In our scheme, the resolution improvement is limited by the NA of both the illumination and detection objective. Thus, the resolution can be further improved by using higher illumination lateral wavevector to extract higher spatial frequency information of the object. For example, localized plasmonic structures have been used to excite the object with higher wavevector for super resolution imaging.[47] In the meantime, since the forward dark field imaging process can be estimated and computed numerically, the network structure can also be modified based on the physical model. Recently, the physics-informed neural networks have been studied to solve the inverse problem with the knowledge of forward process, which can be applied to our scheme to improve the generalization of the network in the future with sacrificed speed of reconstruction due to iterations.[34,35]

Although our technique has good performance on the experimental objects including beads and cells, we have to note that there are still some limitations. During the simulation process, the objects are considered as two-dimensional

objects with isotropic scattering coefficient. This assumption works well with thin objects like beads in Fig. 3 with almost no artifact in the output images. However, when it comes to thicker cell samples, we may miss some information. In this case, scattering of three dimensional structures need to be considered in simulation for better accuracy which will make the simulation more complex.[48,49]

In conclusion, we propose and demonstrate a deep learning based framework specifically designed to enhance the resolution in dark-field microscopy. Simulation datasets containing both low resolution and high resolution images are generated based on only a few parameters of the traditional DFM. A U-net is trained on the simulated dataset to reconstruct super resolution dark-field images from the low-resolution experiment images. The network tested with both simulation data and experiment data shows ~2 times improvement in resolution. One of the major advantages of the proposed technique is that a massive dataset from experiment which is usually required in data-driven neural network is not necessary for training. Thus, with the knowledge of the optical parameters, this technique can be easily applied to any DFM without modification to the setup and doubles the resolution for the label-free dark-field imaging. We believe our technique will benefit biomedical and chemical studies a lot with the easily obtainable resolution enhancements.

Data availability

Data in this work may be obtained from the corresponding author upon reasonable request. Codes are available at **https://github.com/ML-UCSD/DLDFM.git**.

Author contributions

M. L. and Z. L. conceived the project. M. L. performed simulation and all data analysis. M. L. and J. Zhao conducted bead experiments. M. L. and J. Zhou conducted phase target experiments. M. L. and H. L. performed cell experiments. M. L., J. Zhao and J. Zhou wrote the manuscript. All authors discussed and commented on the manuscript. Z. L. supervised the project.

Conflicts of interest

The authors declare no conflicts of interest.

Acknowledgements

This work was supported by the Gordon and Betty Moore Foundation (Grant No. 5722). We acknowledge Woo Joong Rhee and Prof. Jeon-Soo Shin at the Department of Microbiology, Yonsei University College of Medicine for preparing fixed HeLa cells.

References

1 R. E. Leighton, A. M. Alperstein and R. R. Frontiera, *Annu. Rev. Anal. Chem.*, 2022, **15**, 37–55.
2 P. F. Gao, G. Lei and C. Z. Huang, *Anal. Chem.*, 2021, **93**, 4707–4726.
3 T. Horio and H. Hotani, *Nature*, 1986, **321**, 605–607.
4 I. Ishmukhametov, L. Nigamatzyanova, G. Fakhrullina and R. Fakhrullin, *Anal. Bioanal. Chem*, 2022, **414**, 1297–1312.
5 H. Sherman, S. Klausner and W. A. Cook, *Angiology*, 1971, **22**, 295–303.
6 J. Zhou, H. Qian, C.-F. Chen, J. Zhao, G. Li, Q. Wu, H. Luo, S. Wen and Z. Liu, *Proc. Natl. Acad. Sci. U. S. A.*, 2019, **116**, 11137–11140.
7 H. Hu, C. Ma and Z. Liu, *Appl. Phys. Lett.*, 2010, **96**, 113107.
8 J. Zhou, H. Qian, J. Zhao, M. Tang, Q. Wu, M. Lei, H. Luo, S. Wen, S. Chen and Z. Liu, *Natl. Sci. Rev.*, 2021, **8**, nwaa176.
9 J. Ling, Y. Wang, X. Liu and X. Wang, *Opt. Lett.*, 2021, **46**, 1265–1268.
10 E. Betzig, A. Lewis, A. Harootunian, M. Isaacson and E. Kratschmer, *Biophys. J.*, 1986, **49**, 269–279.
11 M. J. Rust, M. Bates and X. Zhuang, *Nat. Methods*, 2006, **3**, 793–796.
12 E. Betzig, G. H. Patterson, R. Sougrat, O. W. Lindwasser, S. Olenych, J. S. Bonifacino, M. W. Davidson, J. Lippincott-Schwartz and H. F. Hess, *Science*, 2006, **313**, 1642–1645.
13 K. I. Willig, S. O. Rizzoli, V. Westphal, R. Jahn and S. W. Hell, *Nature*, 2006, **440**, 935–939.
14 Z. Liu, H. Lee, Y. Xiong, C. Sun and X. Zhang, *Science*, 2007, **315**, 1686–1686.
15 M. G. Gustafsson, *J. Microsc.*, 2000, **198**, 82–87.
16 J. Chen, Y. Xu, X. Lv, X. Lai and S. Zeng, *Opt. Express*, 2013, **21**, 112–121.
17 G. Zheng, R. Horstmeyer and C. Yang, *Nat. Photonics*, 2013, **7**, 739–745.
18 X. Ou, G. Zheng and C. Yang, *Opt. Express*, 2014, **22**, 4960–4972.
19 Y. Rivenson, Z. Göröcs, H. Günaydin, Y. Zhang, H. Wang and A. Ozcan, *Optica*, 2017, **4**, 1437–1443.
20 A. Sinha, J. Lee, S. Li and G. Barbastathis, *Optica*, 2017, **4**, 1117–1125.
21 O. Ronneberger, P. Fischer and T. Brox, U-net: Convolutional networks for biomedical image segmentation, *Medical Image Computing and Computer-Assisted Intervention–MICCAI 2015*, 18th International Conference, Springer International Publishing, Munich, Germany, 2015, 234–241.
22 G. Barbastathis, A. Ozcan and G. Situ, *Optica*, 2019, **6**, 921–943.
23 W. Ma, Z. Liu, Z. A. Kudyshev, A. Boltasseva, W. Cai and Y. Liu, *Nat. Photonics*, 2021, **15**, 77–90.
24 Y. Han, L. Sunwoo and J. C. Ye, *IEEE Trans. Med. Imaging*, 2019, **39**, 377–386.
25 T. Nguyen, Y. Xue, Y. Li, L. Tian and G. Nehmetallah, *Opt. Express*, 2018, **26**, 26470–26484.

26 E. Nehme, L. E. Weiss, T. Michaeli and Y. Shechtman, *Optica*, 2018, **5**, 458–464.
27 Z. Meng, L. Ding, S. Feng, F. Xing, S. Nie, J. Ma, G. Pedrini and C. Yuan, *Opt. Express*, 2020, **28**, 34266–34278.
28 W. Ouyang, A. Aristov, M. Lelek, X. Hao and C. Zimmer, *Nat. Biotechnol.*, 2018, **36**, 460–468.
29 H. Wang, Y. Rivenson, Y. Jin, Z. Wei, R. Gao, H. Günaydın, L. A. Bentolila, C. Kural and A. Ozcan, *Nat. Methods*, 2019, **16**, 103–110.
30 B. Sahiner, A. Pezeshk, L. M. Hadjiiski, X. Wang, K. Drukker, K. H. Cha, R. M. Summers and M. L. Giger, *Med. Phys.*, 2019, **46**, e1–e36.
31 A. A. Mohamed, W. A. Berg, H. Peng, Y. Luo, R. C. Jankowitz and S. Wu, *Med. Phys.*, 2018, **45**, 314–321.
32 F. Wang, C. Wang, C. Deng, S. Han and G. Situ, *Photonics Res.*, 2022, **10**, 104–110.
33 R. Heckel and M. Soltanolkotabi, Compressive sensing with un-trained neural networks: Gradient descent finds a smooth approximation, International Conference on Machine Learning. PMLR, 2020, 4149–4158.
34 F. Wang, Y. Bian, H. Wang, M. Lyu, G. Pedrini, W. Osten, G. Barbastathis and G. Situ, *Light: Sci. Appl.*, 2020, **9**, 1–7.
35 F. Wang, C. Wang, M. Chen, W. Gong, Y. Zhang, S. Han and G. Situ, *Light: Sci. Appl.*, 2022, **11**, 1.
36 M. Karaman, P.-C. Li and M. O'Donnell, *IEEE Trans. Ultrason. Ferroelectr. Freq. Control*, 1995, **42**, 429–442.
37 W. Luo, A. Greenbaum, Y. Zhang and A. Ozcan, *Light: Sci. Appl.*, 2015, **4**, e261–e261.
38 A. Lucas, M. Iliadis, R. Molina and A. K. Katsaggelos, *IEEE Signal Process. Mag.*, 2018, **35**, 20–36.
39 J. Adler and O. Öktem, *Inverse Probl.*, 2017, **33**, 124007.
40 S. Li, M. Deng, J. Lee, A. Sinha and G. Barbastathis, *Optica*, 2018, **5**, 803–813.
41 F. Lv, Y. Li and F. Lu, *Int. J. Comput. Vis.*, 2021, **129**, 2175–2193.
42 W. Ma, F. Cheng and Y. Liu, *ACS Nano*, 2018, **12**, 6326–6334.
43 X. Glorot, A. Bordes and Y. Bengio, Deep sparse rectifier neural networks, Proceedings of the fourteenth international conference on artificial intelligence and statistics, JMLR Workshop and Conference Proceedings, 2011, 315–323.
44 D. P. Kingma and J. Ba, 2014, arXiv preprint arXiv:.
45 H. Zhao, O. Gallo, I. Frosio and J. Kautz, *IEEE Trans. Comput. Imaging*, 2016, **3**, 47–57.
46 J. Darbon, A. Cunha, T. F. Chan, *et al.*, Fast nonlocal filtering applied to electron cryomicroscopy, 2008 5th IEEE International Symposium on biomedical imaging: from nano to macro. *IEEE*, 2008, 1331–1334.
47 J. L. Ponsetto, F. Wei and Z. Liu, *Nanoscale*, 2014, **6**, 5807–5812.
48 J. Q. Lu, P. Yang and X.-H. Hu, *J. Biomed. Opt.*, 2005, **10**, 024022.
49 T. Wriedt, *J. Quant. Spectrosc. Radiat. Transfer*, 2009, **110**, 833–843.